Inclusive Diffraction at HERA*

Henri Kowalski

Deutsches Elektronen Synchrotron DESY, 22603 Hamburg, Germany

Abstract. Diffractive phenomena observed at HERA are starting to give us a new perspective on the deep inelastic scattering. In this talk the properties of diffractive events observed by the H1 and ZEUS experiments are described. We give also a theoretical interpretation of the diffractive results with special emphasis on the phenomena at the boundary of soft and hard physics. In this region perturbative QCD seems to provide a useful guide. Simple models can be constructed which allow to connect the photoproduction, deep inelastic scattering and diffractive phenomena in a quantitative way.

1 Introduction

One of the most important results of the experiments at HERA is the observation that a substantial amount ($\sim 10\%$) of deep-inelastic electron-proton scattering (DIS) events is of diffractive origin. The usual DIS events are characterized by continuous particle emission between the direction of the struck quark and the proton remnant. In the γ^*-proton rest frame this leads to an almost uniform distribution of emitted particles along the $\gamma^* p$ rapidity axis, The rapidity interval in which particles are radiated has the length $\ln W^2$, where W denotes the $\gamma^* p$ CMS energy in GeV. Diffractive processes are characterized by particle emission in a considerably shorter rapidity interval given by $\ln M_X^2$, where M_X denotes

* Presented at *New Trends in HERA Physics 1999*, Ringberg Workshop, June 1999

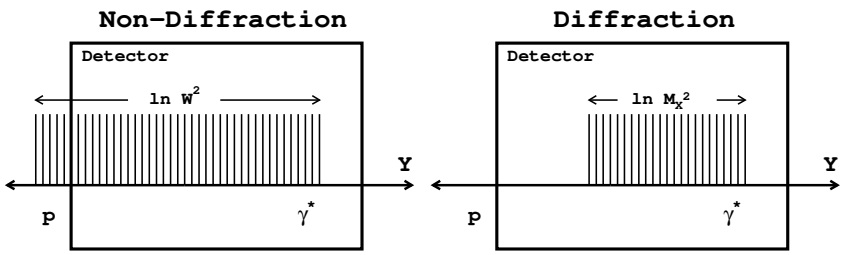

Fig. 1. Particle emission characteristics for non-diffractive (left) and diffractive events (right).

the diffractive mass, see Fig. 1. The mass M_X, which is equal to the invariant mass of all particles emitted in the reaction with exception of the outgoing proton (or the proton dissociated system), is in diffractive reactions considerably smaller than W. Therefore diffractive events exhibit clear rapidity gaps, given by $\Delta Y = \ln W^2 / \ln M_X^2$, [1].

The relatively small amount of hadronic radiation emitted in diffractive reactions is due to the dominance of the colour singlet exchange; this is in contrast to non-diffractive $\gamma^* p$ interactions where coloured gluon exchanges dominate. Diffraction gives new insight into deep inelastic electron proton interactions and gives hope that, because a hard scale is involved, more can be learned about a possible partonic mechanism of diffraction and, eventually, about the transition between the perturbative and nonperturbative regimes.

I will first describe the diffractive measurement and then discuss a possible theoretical interpretation.

2 Diffractive Measurement

2.1 Kinematics

The kinematic quantities used for the description of inclusive DIS, $e(k)+p(P) \to e(k') + anything$, see Fig. 2, are $Q^2 = -q^2 = -(k-k')^2$, $x = Q^2/(2P \cdot q)$, $y = (P \cdot q)/(P \cdot k)$ and $W^2 = Q^2(1-x)/x + m_p^2 \approx Q^2/x$ for $x \ll 1$. Here k, k' are the four-momenta of the initial and final state positrons; P is the four-momentum of the intial state proton and y is the fractional energy transfer to the proton in its rest frame. For the range of Q^2 and W considered in this talk $W^2 \approx ys$, where $s = 4E_e E_p$ is the square of the ep c.m.s. energy, $\sqrt{s} = 300$ GeV. The scaling variables used to describe DIS diffraction are given by $x_{I\!P} = [(P-N)\cdot q]/(P \cdot q) \approx$

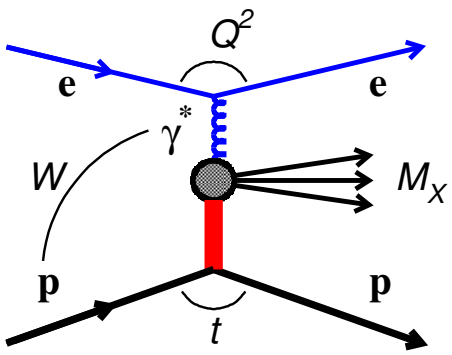

Fig. 2. Diagram showing the diffractive dissociation process in DIS.

$(M_X^2 + Q^2)/(W^2 + Q^2)$ and $\beta = Q^2/[2(P-N)\cdot q] = x/x_{I\!P} \approx Q^2/(M_X^2 + Q^2)$ where N is the four-momentum of the outgoing nucleonic system and M_X is the mass of the system into which the virtual photon dissociated. In models where diffraction is described by the t-channel exchange of a system, for example the pomeron, $x_{I\!P}$ is the momentum fraction of the proton carried by this system and β is the momentum fraction of the struck quark within this system.

2.2 Diffractive Signature

The diffractive and non-diffractive components can be experimentally separated by the analysis of the observed M_X distribution [2,3]. Fig. 3 shows these distributions in terms of $\ln M_X^2$ for various W intervals as observed in the ZEUS detector. The high mass peak is due to non-diffractive events, the plateau-like structure most notably seen at higher W values, is due to diffractive ones. The high mass peak has a steep exponential fall-off, $d\mathcal{N}/d\ln M_X^2 \propto \exp(b \ln M_X^2)$, towards smaller $\ln M_X^2$ values. The position of the high mass peak changes proportionally to $\ln W^2$, i.e. shows scaling in $\ln(M_X^2/W^2)$ and the slope, b, of the exponential in $\ln M_X^2$ is approximately independent of W and Q^2. These characteristics are properties of events with uniform, random and uncorrelated particle production along the rapidity axis where, due to the geometrical acceptance of the detector, particles are measured in a limited range of rapidity, see Fig. 1 . In models such as the Feynman gas model or ones dominated by longitudinal phase space [1], the slope b represents the particle multiplicity per unit of rapidity. The exponential in $\ln M_X^2$ and the scaling in $\ln(M_X^2/W^2)$ are directly connected to the exponential suppression of large rapidity gaps by QCD radiation.

These characteristics are also properties of realistic models for particle production in deep inelastic scattering. ARIADNE [4], which gives a good descrip-

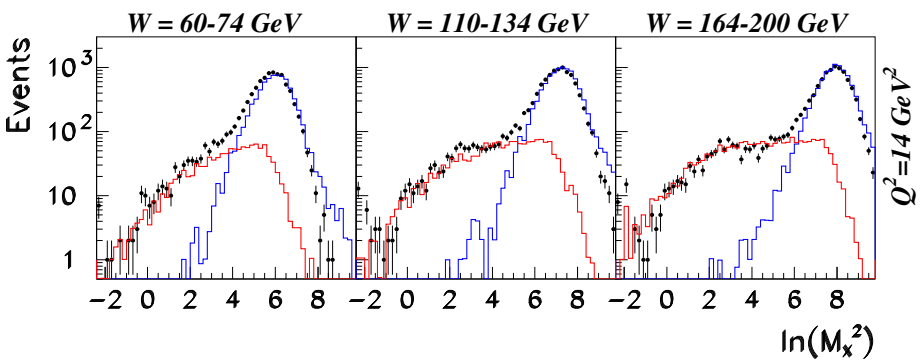

Fig. 3. Distribution of M_X in terms of $\ln M_X^2$. The solid points show the data. The solid histograms show the ARIADNE predictions for non-diffractive reactions. The dashed histograms show the predictions of RAPGAP for diffractive reactions.

tion of particle production by DIS at HERA, also exhibits a pure exponential fall-off with $\ln M_X^2$ and scaling in $\ln M_X^2/W^2$. The distribution predicted by ARIADNE shown in Fig. 3 gives a good account of the high mass peak. The plateau-like part of the $\ln M_X^2$ distribution in Fig. 3 is well described by the diffractive RAPGAP simulation.

2.3 Selection of Diffractive Events

In diffractive events, the system X resulting from the dissociation of the virtual photon is almost fully contained in the detector while the outgoing proton or low mass nucleonic system escapes through the forward beam hole. Diffractive dissociation prefers small M_X values and leads to an event distribution of the form $d\mathcal{N}/dM_X^2 \propto 1/(M_X^2)^{(1+n)}$ corresponding to $d\mathcal{N}/d\ln M_X^2 \propto 1/(M_X^2)^n$, approximately independent of W. At high energies and for large M_X, one expects $n \approx 0$, leading to a constant distribution in $\ln M_X^2$, as discussed below.

In the ZEUS investigation [3] the diffractive contribution was identified as the excess of events at small M_X above the exponential fall-off of the nondiffractive contribution in $\ln M_X^2$. This method is called the M_X method for the determination of the diffractive component and was developed by H. Kowalski and G. Wolf. The exponential fall-off permits the subtraction of the nondiffractive contribution and, therefore, the extraction of the diffractive contribution without assuming the precise M_X dependence of the latter. The $\ln M_X^2$ distribution for both contributions together is expected to be of the form:

$$\frac{d\mathcal{N}}{d\,\ln M_X^2} = D + c\,\exp(b\,\ln M_X^2), \qquad \text{for} \quad \ln M_X^2 \leq \ln W^2 - \eta_0. \tag{1}$$

Here, D denotes the diffractive contribution and the second term the nondiffractive contribution. The diffractive term D is corrected for the detector distortion

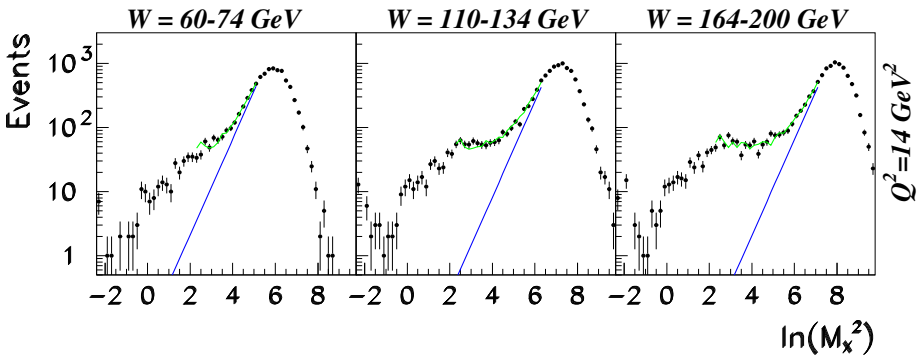

Fig. 4. Distribution of M_X in terms of $\ln M_X^2$. The straight lines give the non-diffractive contribution as obtained from the fits.

effects. The nondiffractive term is not corrected since the detector effects on the exponential fall-off were found to be negligible. The quantity $(\ln W^2 - \eta_0)$ specifies the maximum value of $\ln M_X^2$ up to which the exponential behaviour of the nondiffractive part holds. Its value was determined from the data [3]. The diffractive contribution is not taken from the fit result for D but is determined by subtracting from the observed number of events the nondiffractive contribution found from the fit values of b and c, see Fig. 4. The M_X method selects diffractive events in which the system N, emitted close to the direction of the incoming proton, escapes undetected. Detector acceptance limits the mass of the system N to $M_N < 5.5\ GeV$.

In the H1 investigation [5] the selection of diffractive events was performed by the requirement of a large rapidity gap in the event. This selection makes use of the information from the central and various forward detectors. The particles observed for each event are grouped into two systems, called Y and N, such that the maximum rapidity gap observed is between Y and N. The system N, which includes particles produced in the direction of the incoming proton is required to have a mass $M_N < 1.6\ GeV$. The presence of forward detectors allows H1 to extend the diffractive measurement beyond the region accessible to the ZEUS M_X measurement.

The ZEUS M_X and the H1 rapidity gap methods allow only to measure the diffractive cross section integrated over the four-momentum transfer t. The t dependence of the diffractive cross section was measured by the ZEUS leading proton spectrometer (LPS) [6]. The LPS is designed to measure small angle ($\sim$ 1 mrad) scattered protons which would otherwise escape undetected inside the beam pipe. Isolation of diffractive events with the LPS is rather straight forward: detection of a proton carrying a large fraction of the momentum of the incoming proton, $x_L = p^{LPS}/p_{p_{beam}} > 0.97$, ensures a large rapidity gap between the outgoing proton and the system X. However, the event rate is considerably limited by the acceptance of the LPS.

2.4 Results

The cross section for the virtual photoproduction process $\gamma^* p \to XN$ can be determined from corresponding cross sections for $ep \to eXN$ by:

$$\frac{d\sigma^{diff}_{\gamma^* p \to XN}(M_X, W, Q^2)}{dM_X} \approx \frac{2\pi}{\alpha} \frac{Q^2}{(1-y)^2+1} \frac{d\sigma^{diff}_{ep \to eXN}(M_X, W, Q^2)}{dM_X d\ln W^2 dQ^2} \qquad (2)$$

The diffractive cross section determined by ZEUS is shown in Fig. 5 as a function of W for various M_X and Q^2 values [3]. We observe a rapid rise of the cross section with W at all Q^2 values for the M_X bins up to 7.5 GeV.

The differential γp cross section is related to the diffractive structure function, $F_2^{D(3)}(\beta, x_{I\!P}, Q^2)$, by

$$\frac{1}{2M_X} \frac{d\sigma^{diff}_{\gamma^* p \to XN}(M_X, W, Q^2)}{dM_X} \approx \frac{4\pi^2\alpha}{Q^2(Q^2+M_X^2)} x_{I\!P} F_2^{D(3)}(\beta, x_{I\!P}, Q^2). \qquad (3)$$

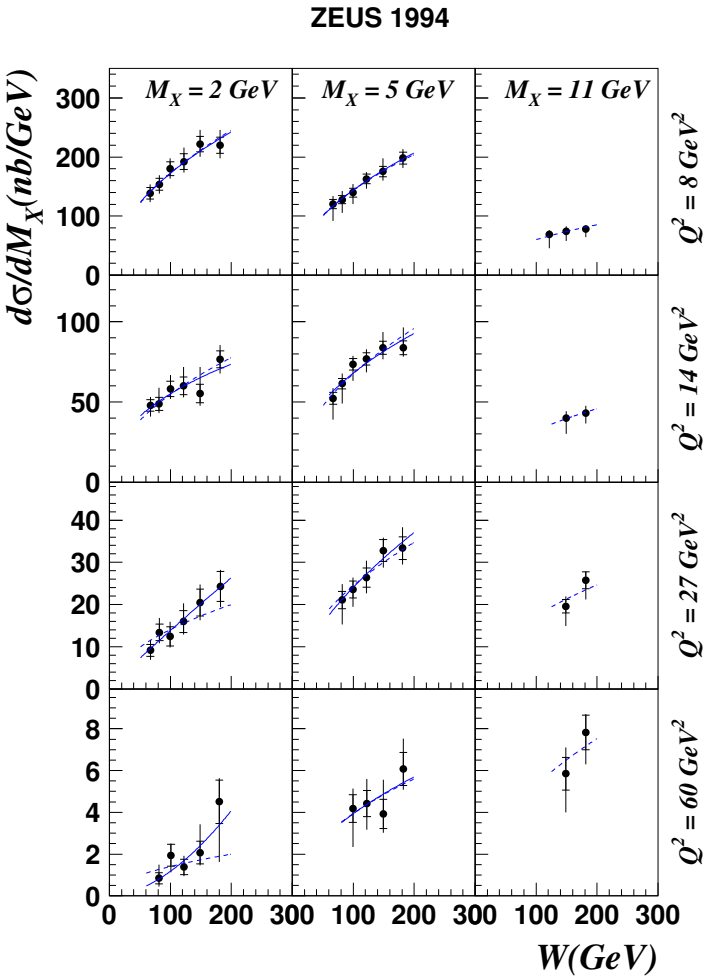

Fig. 5. The differential cross sections $d\sigma^{diff}_{\gamma^* p\to XN}/dM_X$, $M_N < 5.5$ GeV, as a function of W at various M_X values. The inner error bars show the statistical errors and the full bars the statistical and systematic errors added in quadrature. The solid curves show the result from fitting the diffractive cross section for each (W, Q^2) bin separately using the form $d\sigma^{diff}_{\gamma^* p\to XN}/dM_X \propto (W^2)^{a^{diff}}$ where a^{diff} and the normalization constants were treated as free parameters. The dashed curves show the result from the fit where a^{diff} was assumed to be the same for all (W, Q^2) bins.

If $F_2^{D(3)}$ is interpreted in terms of quark densities then it specifies for a diffractive process the probability to find a quark carrying a momentum fraction $x = \beta x_{I\!P}$ of the proton momentum, with x being the Bjorken x.

The H1 results are shown in Fig. 6 in terms of diffractive structure function, $x_{I\!P} F_2^{D(3)}(\beta, x_{I\!P}, Q^2)$ as a function of $x_{I\!P}$ at various β and Q^2 values [5]. The quick rise with W observed in the diffractive cross section measurment corresponds here to the rise of $x_{I\!P} F_2^{D(3)}$ with decreasing $x_{I\!P}$.

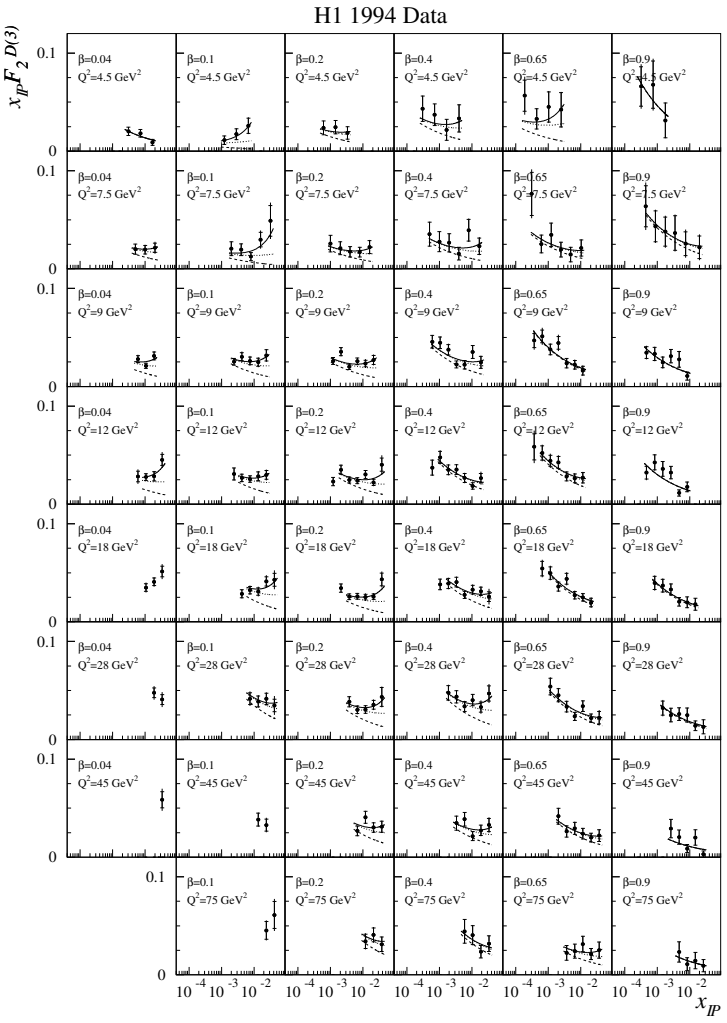

Fig. 6. The solid points show the measured differential structure function plotted as $x_{I\!P} F_2^{D(3)}(\beta, x_{I\!P}, Q^2)$ against $x_{I\!P}$ for various β and Q^2 values. The inner error bars represent the statistical errors and the outer error bars represent the statistical and systematic error added in quadrature. The solid curves show the results of the Regge fit described in text. The dashed curves give the contributions of the pomeron alone and the pomeron with the interfence term.

One of the most important results obtained from the diffractive measurement was the observation that the diffractive cross section rises rapidly with W at all Q^2 values and the measurement of its rate of rise. In the ZEUS case the cross section was fitted for each (M_X, Q^2) bin using the form

$$\frac{d\sigma^{diff}_{\gamma^* p \to XN}(M_X, W, Q^2)}{dM_X} = h \cdot W^{a^{diff}} \quad , \tag{4}$$

where a^{diff} and the normalization constants h were treated as free parameters. In Regge models, a^{diff} is related to the trajectory of the pomeron $\alpha_{I\!P}(t)$, averaged over t: $\overline{\alpha_{I\!P}} = 1 + a^{diff}/4$. The fit value for a^{diff} leads to $\overline{\alpha_{I\!P}} = 1.127 \pm 0.009(stat)^{+0.039}_{-0.012}(syst)$.

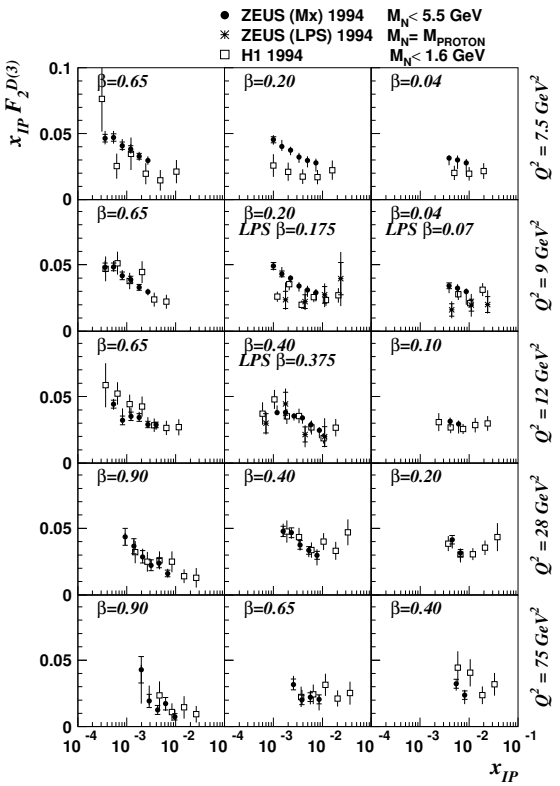

Fig. 7. The diffractive structure function of the proton for $\gamma^* p \to XN, M_N < 5.5$ GeV, multiplied by $x_{I\!P}$, $x_{I\!P} F_2^{D(3)}(x_{I\!P}, \beta, Q^2)$, from the M_X analysis (solid points) compared with the results from ZEUS LPS measurement obtained with an identified proton for $\gamma^* p \to Xp$ (stars) and from a subsample of the H1 data (open points) for $\gamma^* p \to XN, M_N < 1.6$ GeV.

In the H1 case, due to the larger kinematic region accessed by the measurement, $F_2^{D(3)}(\beta, x_{I\!P}, Q^2)$ was fitted using a combined pomeron and reggeon ansatz,

$$F_2^{D(3)}(\beta, x_{I\!P}, Q^2) = c_1 (1/x_{I\!P})^{2\alpha_{I\!P}-1} + c_2 (1/x_{I\!P})^{2\alpha_{I\!R}-1} \qquad (5)$$

H1 [5] has given for the intercept of the pomeron trajectory a value of $\alpha_{I\!P}(0) = 1.203 \pm 0.020(stat) \pm 0.013(syst)^{+0.030}_{-0.035}(model)$. Averaging over the t-distribution gives approximately $\overline{\alpha_{I\!P}} = \alpha_{I\!P}(0) - 0.03$, a value which is in agreement with the ZEUS result.

The $\alpha_{I\!P}$ values of both experiments lie above the $\alpha_{I\!P}$ values deduced from hadron-hadron scattering, where the intercept of the pomeron trajectory was found to be $\alpha_{I\!P}{}^{soft}(0) = 1.08$ [14]. Averaging over t reduces this value by about 0.02 leading to $\overline{\alpha_{I\!P}}^{soft} = 1.06$ [14].

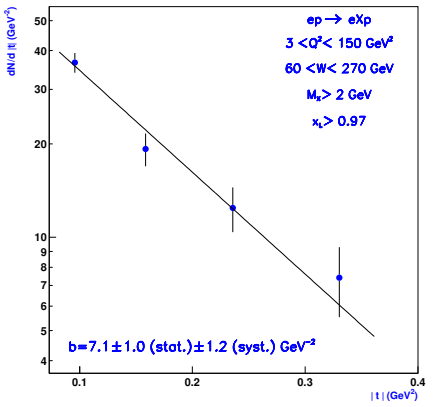

Fig. 8. $|t|$-dependence of the diffractive cross section as measured by the ZEUS collaboration.

In Fig. 7 the data from the ZEUS M_X analysis (solid points) are compared with ZEUS data obtained using the LPS [15] and with those of H1 [5]. For ease of comparison the $x_{I\!P} F_2^{D(3)}$ values from this analysis were scaled to the (β, Q^2) values used in the H1 analysis. The LPS data correspond to events of the type $\gamma^* p \to Xp$ with an identified proton. No correction was applied for the contribution from double dissociation which is present in the ZEUS M_X analysis but not in the LPS data. The correction would increase the LPS data by a factor of $1.45^{+0.40}_{-0.26}$. There is consistency between the M_X analysis and the LPS data. The H1 data correspond to $M_N < 1.6$ GeV while those from the M_X analysis are given for $M_N < 5.5$ GeV. No correction was applied. The data from H1 approximately agree with those from the ZEUS M_X analysis. However, for fixed

β, the H1 values have a tendency to rise faster with Q^2 even allowing for an extra scaling factor.

The dependence of the diffractive cross section $d\sigma_{\gamma^* p \to X_p}/dM_X$ on the square of the four-momentum transfer t is shown in Fig. 8 The cross section is steeply falling with $-t$, $d\sigma/dt \propto \exp(bt)$ with $b = 7.1 \pm 1.(stat) \pm 1.2(syst)$. This shows that small momentum transfers between incoming and outgoing proton dominate as expected for diffractive scattering.

3 Theoretical Interpretation

In the parton model the DIS process, $\gamma^* p \to XN$, can be visualized, in the rest frame of the proton, as a fluctuation of the incoming virtual photon into a $q\overline{q}$ pair followed by the interaction of this pair with the incoming proton [7,8]. In a diffractive DIS process the final state will be particularly simple: it consists of a $q\overline{q}$ state plus a proton or debris from the dissociation of the proton, well separated in rapidity.

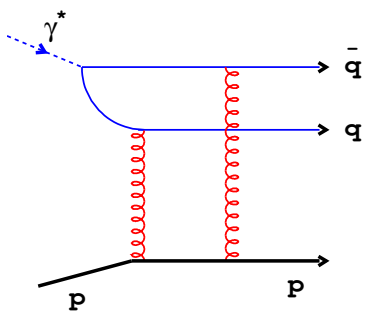

Fig. 9. Feynman diagram describing the fluctuation of $\gamma^* \to q\overline{q}$ with subsequent scattering by two gluon exchange on the proton

Some thirty years ago, J.D. Bjorken has pointed out that configurations with small q (or $\overline{q}$) transverse momenta relative to the direction of the virtual photon will lead to a substantial diffractive cross section in DIS [9]. Therefore, since in general one of the quarks of the pair will have a large logitudinal momentum, the so called aligned jet configuration will dominate. The cross section for this configuration is expected to scale with Q^2 and to have the same W dependence as observed for diffraction in hadron-hadron scattering.

The aligned jet model can be, today, well understood within QCD [10,12]. In diffraction, the interaction of the proton with a quark pair is mediated by the

exchange of a colour singlet gluonic system. Such a system cannot resolve a $q\overline{q}$ (neutral) pair when the typical wave length of a gluon is larger than the $q\overline{q}$ pair transverse separation. Since the colour force which binds the proton has a wave length of the order of the proton size only pairs with small transverse momenta will interact with the proton.

The β distribution of the aligned quark configuration from transverse photons was predicted, by A. Donnachie and P.V. Landshoff [13], to be of the form

$$F_{q\overline{q}}^{T} \propto \beta(1-\beta). \tag{6}$$

N.N. Nikolaev and B.G. Zakharov have shown that the same β dependence was expected in pQCD when the aligned quarks interact with the proton through two-gluon exchange [16].

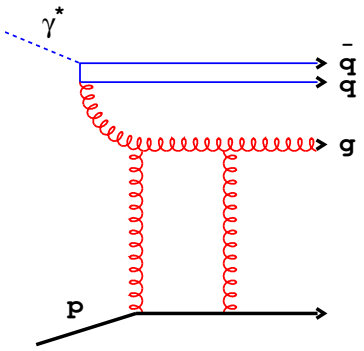

Fig. 10. Feynman diagram describing the fluctuation of $\gamma^* \to q\overline{q}g$ with subsequent scattering by two gluon exchange on the proton

The production of a $q\overline{q}g$ system by transverse photons was found by N.N. Nikolaev and B.G. Zakharov to be also of leading twist and was assumed to have a β dependence of the type [16]

$$F_{q\overline{q}g}^{T} \propto (1-\beta)^{\gamma} \tag{7}$$

with $\gamma = 2$. A later calculation by M. Wüsthoff [17] found $\gamma = 3$.

The contribution to the production of a $q\overline{q}$ system by longitudinal photons was found to be of higher twist and to have a β dependence of the form [17]

$$F_{q\overline{q}}^{L} \propto \beta^3(1-2\beta)^2. \tag{8}$$

In pQCD models the $x_{I\!P}$ dependence is expected to be driven by the x dependence of the square of the gluon momentum density of the proton [18], $[x \cdot g(x,\mu^2)]^2$, with $x = x_{I\!P}$ and μ the probing scale.

3.1 BEKW Model

J. Bartels, J. Ellis, H. Kowalski and M. Wüsthoff (BEKW) indentified the theoretical processes leading to the three terms in eqs. 6- 8 as the major contributors to the diffractive structure function. In [10] the three contributions were calculated in the perturbative region and extended into the soft region. The $x_{I\!P}$ dependence was assumed to be of the form $(1/x_{I\!P})^n$. The power n was allowed to be different for the transverse (n_T) and the longitudinal (n_L) contributions.

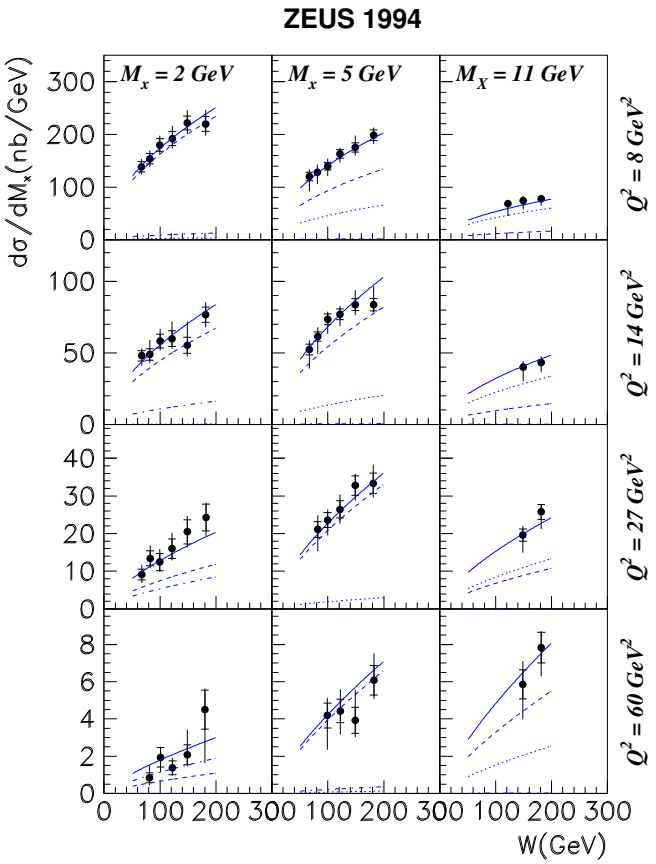

Fig. 11. Comparison of the ZEUS M_X data with the results of the BEKW fit (solid curve). The transverse $q\overline{q}$ contribution is shown by the dashed curve, the longitudinal $q\overline{q}$ contribution by the dashed-dotted curve and the transverse $q\overline{q}g$ contribution by the dotted line.

The normalizations of the three terms were determined from the data:

$$x_{I\!P} F_2^{D(3)}(\beta, x_{I\!P}, Q^2) = c_T \cdot F_{q\overline{q}}^T + c_L \cdot F_{q\overline{q}}^L + c_g \cdot F_{q\overline{q}g}^T \qquad (9)$$

with

$$F_{q\bar{q}}^{T} = (\frac{x_0}{x_{I\!P}})^{n_T(Q^2)} \cdot \beta(1-\beta) \tag{10}$$

$$F_{q\bar{q}}^{L} = (\frac{x_0}{x_{I\!P}})^{n_L(Q^2)} \cdot \frac{Q_0^2}{Q^2} \cdot [\ln(\frac{7}{4} + \frac{Q^2}{4\beta Q_0^2})]^2 \cdot \beta^3(1-2\beta)^2 \tag{11}$$

$$F_{q\bar{q}g}^{T} = (\frac{x_0}{x_{I\!P}})^{n_T(Q^2)} \cdot \ln(1+\frac{Q^2}{Q_0^2}) \cdot (1-\beta)^{\gamma} \tag{12}$$

$$n_{T,L}(Q^2) = 0.1 + n_{T,L}^0 \cdot \ln[1+\ln(\frac{Q^2}{Q_0^2})]. \tag{13}$$

The three terms have different Q^2 dependences. $F_{q\bar{q}}^{T}$ does almost not depend on Q^2 as a result of the limited quark p_T in the aligned configuration. The term $F_{q\bar{q}}^{L}$ is higher twist but the power $1/Q^2$ is softened by a logarithmic Q^2 factor; $F_{q\bar{q}g}^{T}$ grows logarithmically with Q^2 similar to the proton structure function F_2 at low x.

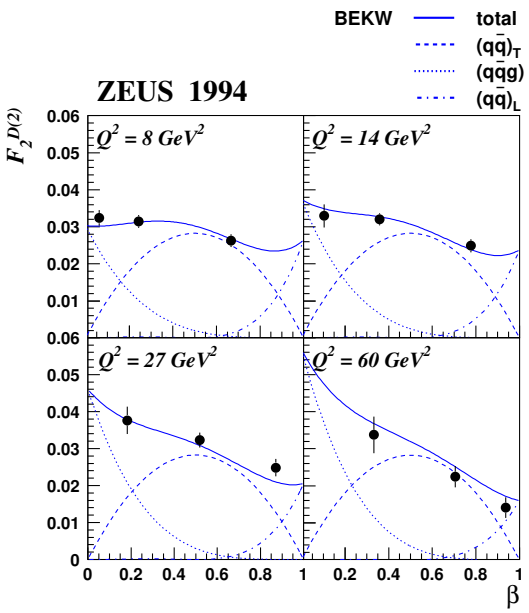

Fig. 12. Comparison of the $F_2^{D(2)}$ with the results of the BEKW fit.

The coefficients c_T, c_L, c_g as well as the parameters n_T^0, n_L^0 and x_0, Q_0^2 were determined from experiment. In the fit the power γ was also considered as a free parameter. Assuming $Q_0^2 = 1$ GeV^2 and $x_0 = 0.0042$ and treating the other constants as free parameters a good fit ($\chi^2/d.o.f. = 56/47 = 1.2$, statistical

errors only) was obtained for the ZEUS M_X data as shown by the solid curves in Fig. 11. The fit yielded the following parameter values: $n_T^0 = 0.13 \pm 0.03$, $n_L^0 = 0.32 \pm 0.14$, $\gamma = 3.9 \pm 0.9$ [3]. It is instructive to compare the β dependence of the three components which build up the diffractive structure function using the results from the BEKW fit as shown in Fig. 12.[1] The ZEUS data suggest that for $\beta > 0.2$ the colourless system couples predominantly to the quarks in the virtual photon. The region $\beta \geq 0.8$ is dominated by the contributions from longitudinal photons. The contribution from coupling of the colourless system to a $q\overline{q}g$ final state becomes important for $\beta < 0.3$. Figure 13 shows the same quantities as

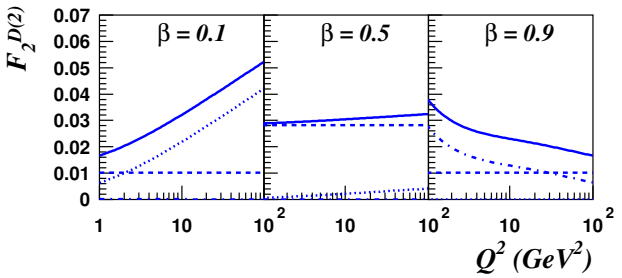

Fig. 13. $F_2^{D(2)}$ obtained from the BEKW fit to the ZEUS M_X data as a function of Q^2

a function of Q^2 for $\beta = 0.1, 0.5, 0.9$. One finds within the BEKW model and using ZEUS data, that the gluon term, which dominates at $\beta = 0.1$ rises with Q^2 while the quark term, which is important at $\beta = 0.5$ shows almost no evolution with Q^2. The contribution from longitudinal photons, which is higher twist and dominates at $\beta = 0.9$, decreases with Q^2.

In the BEKW model the $x_{I\!P}$-dependence of the quark and gluon contributions for transverse photons is expected to be close to that given by the soft pomeron, $n_T \approx 2(\overline{\alpha_{I\!P}}^{soft} - 1)$. However, perturbative admixtures in the diffractive final state are expected to have a somewhat stronger energy dependence, leading to an effective $n_T > 2(\overline{\alpha_{I\!P}}^{soft} - 1)$. The $x_{I\!P}$ dependence of the longitudinal contribution is driven by the square of the proton's gluon momentum density leading to $n_L > n_T$. The fit results agree with these predictions but the errors are too large for a definitive statement.

Similar fits were performed to H1 data [10]. In the H1 case the data allowed two, from the χ^2 point of view, almost equivalent solutions. One with the value of the parameter $\gamma = 0.28 \pm 0.08$ and another with $\gamma = 8.5 \pm 0.8$. The high γ solution leads to conclusions which are similar to those obtained from the ZEUS

[1] $F_2^{D(2)}$ denotes $F_2^{D(3)}$ at $x_{I\!P} = x_0$

data analysis. In the low γ solution the gluon term is dominant at large β region, which is in agreement with the H1 analysis [5] based on a DGLAP NLO fit.

3.2 Saturation Model

A.H. Mueller in his DIS 98 talk at Brussel [19] drew attention to the fact that the much stronger rise with W of the diffractive cross section in DIS as compared to hadron-hadron scattering combined with the behaviour of the F_2 data suggests the presence of saturation in DIS processes. Motivated by this talk K. Golec-Biernat with M. Wüsthoff developed a model which connects in a quantitative way the low and higher Q^2 total cross section data with the inclusive diffractive process [20,21]. Similar models were also proposed by J.R. Forshaw et al. [11] and W. Buchmüller et al. [12].

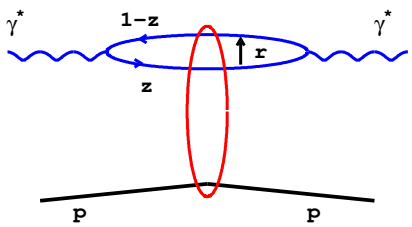

Fig. 14. Diagram of the basic saturation model process

In a frame, where photon and proton are collinear, the total γp and the differential diffractive cross section can be written as [7,8]:

$$\sigma_{T,L}(x,Q^2) = \int d^2\boldsymbol{r} \int dz \, |\Psi_{T,L}(z,\boldsymbol{r})|^2 \, \hat{\sigma}(x,r^2) \tag{14}$$

$$\frac{d\sigma^{Diff}_{T,L}}{dt}|_{t=0} = \frac{1}{16\pi} \int d^2\boldsymbol{r} \int dz \, |\Psi_{T,L}(z,\boldsymbol{r})|^2 \, |\hat{\sigma}(x,r^2)|^2 \tag{15}$$

where $\Psi_{T,L}(z,\boldsymbol{r})|$ denotes the transverse (T) and longitudinally (L) polarized photon wave functions, $\hat{\sigma}(x,r^2)$ the dipole cross section of the $q\overline{q}$ pair with the proton, z the momentum fraction of the photon carried by the quark and r the relative transverse separation between the quarks. The wave functions are solely determined by the coupling of the photon to the quark and therefore are well

known in QCD [8]. The cross section of the $q\overline{q}$ pair with the proton is assumed to be a function of the transverse separation r and the saturation radius R_0:

$$\hat{\sigma}(x, r^2) = \sigma_0 \left(1 - \exp[-\frac{r^2}{4R_0^2}]\right) \tag{16}$$

At small r, $r \ll 2\,R_0$, the dipole cross section grows quadratically with r, $\hat{\sigma} \sim \sigma_0 r^2/4R_0^2$, at large r, $r \gg 2\,R_0$, it saturates, $\hat{\sigma} = \sigma_0$.

The wave function, $\Psi(r)$, at small quark transverse separation, $r < 1/Q$, behaves as $Q \cdot 1/(Qr)$, whereas for large quark transverse separation, $r > 1/Q$, it is exponentially suppressed. When the transverse size of the $q\overline{q}$ pairs is much smaller than the saturation radius, $1/Q \ll R_0$, the total cross section behaves as:

$$\sigma_T = \int dz \int_0^{1/Q^2} dr^2 Q^2 \left(\frac{1}{Q^2 r^2}\right) \sigma_0 \frac{r^2}{4R_0^2} \sim \frac{1}{Q^2}\frac{\sigma_0}{R_0^2} \tag{17}$$

When the transverse size of the $q\overline{q}$ pairs exceeds the saturation radius, $1/Q \gg R_0$, the integration over dr^2 splits into two parts:

$$\sigma_T = \int_0^{R_0^2} dr^2 \left(\frac{1}{r^2}\right) \sigma_0 \frac{r^2}{4R_0^2} + \int_{R_0^2}^{1/Q^2} dr^2 \left(\frac{1}{r^2}\right) \sigma_0 \sim \sigma_0 + \sigma_0 \ln\left(\frac{1}{Q^2\,R_0^2}\right)$$

and σ_T becomes almost independent of Q^2. From the above approximative arguments it can be seen that the model describes the well known scaling behaviour at higher Q^2, $\sigma_T \sim 1/Q^2$, and the break down of scaling at low Q^2, $\sigma_T \sim \sigma_0$.

In order to describe the W (or x) dependence of the total DIS cross sections measured at HERA, the saturation radius has to be x dependent.

$$R_0^2(x) = \frac{1}{Q_0^2}\left(\frac{x}{x_0}\right)^{\lambda} \tag{18}$$

with $Q_0 = 1$ GeV. The eqs. 14, 15, 16 and 18 define the model called in the following the saturation model.

The parameters of the model σ_0, x_0 and λ where determined from the fit to the HERA total cross section data. Figure 15 shows the HERA total cross section data in the Q^2 region between 0.1 and 100 GeV^2 and compares them to the fit. Note that a very good description is achieved for the transition between the photoproduction-like region at $Q^2 < 1GeV^2$ and the scaling region at higher Q^2. The parameters of the model are determined as $\sigma_0 = 23$ (mb), $\lambda = 0.29$, $x_0 = 0.0003$. The value of σ_0 is mainly determined by the behaviour of the data in the photoproduction-like region while λ and x_0 is mainly determined by the DIS region. Note that σ_0, which in the model corresponds to the $q\overline{q}$ proton cross section, is of the same magnitude as the total $\pi^{\pm}p$ cross section.

The results of the saturation model are compared with the data in Fig. 16. We see a good agreement with data at all Q^2 and M_X values, similar in quality

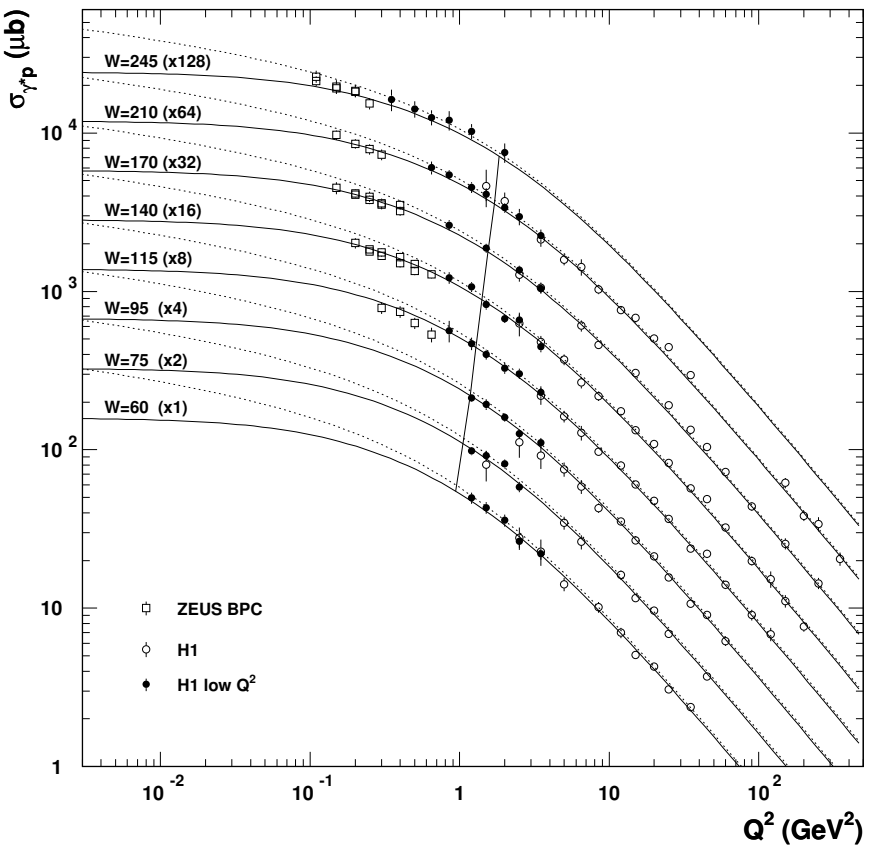

Fig. 15. The $\gamma^* p$ cross section compared to the results of the saturation model fit (solid line). The dotted line shows an alternative fit in which the quark mass was set to zero.

to the BEKW fit as seen in Fig. 11. The difference is that it is now an absolute prediction and not a fit. All parameters of the model were fixed by F_2 data.

It is interesting to compare the data on the ratio of the diffractive and total cross sections with the predictions of the saturation model as shown in Fig. 17. When this ratio was first published the data were difficult to understand since the diffractive and total cross sections show the same rate of growth with W. This is contrary to the naïve expectation that according to the optical theorem the diffractive cross section should grow with a power of W which is twice the power of the total one, $\sigma_{Diff} \sim W^{2a}$ while $\sigma_{TOT} \sim W^a$. This basic property is also present in the saturation model; note that the dipole cross section, $\hat{\sigma}$, appears in quadrature in the equation 15 while only one power of $\hat{\sigma}$ enters equation 14. Therefore, if $\hat{\sigma}$ leads to a growth of the total cross secton with the power λ,

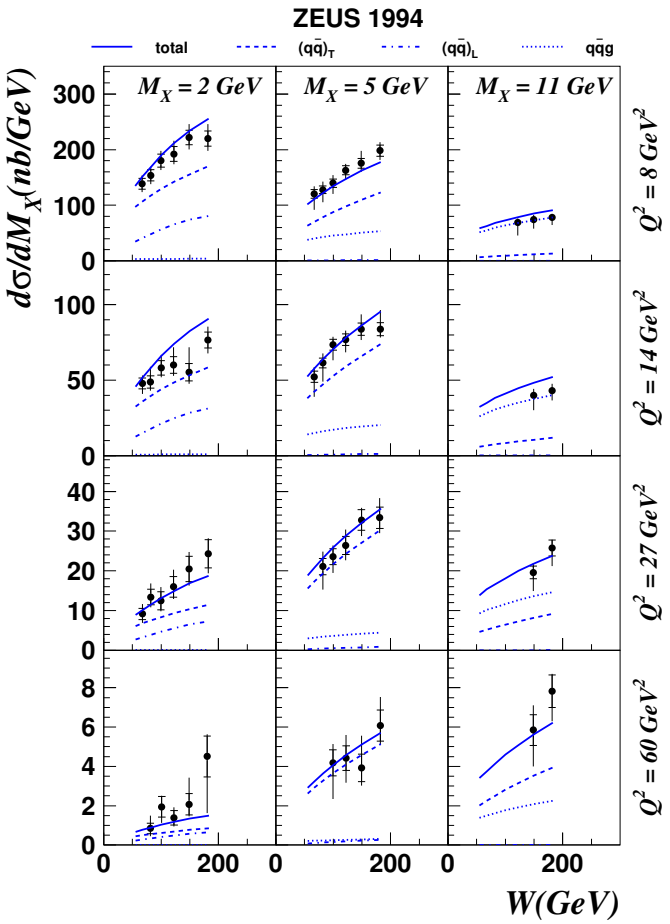

Fig. 16. Comparison of the ZEUS M_X data with the results of the saturation model (solid curve). The transverse $q\overline{q}$ contribution is shown by the dashed curve, the longitudinal $q\overline{q}$ contribution by the dashed-dotted curve and the transverse $q\overline{q}g$ contribution by the dotted line.

$\sigma_T \sim W^\lambda$, (see eqs. 17, 18) then the diffractive cross section would, again, be expected to grow with the power 2λ. The saturation model leads, however, to a remarkably good description of the experimentally observed $\sigma_{Diff}/\sigma_{TOT}$ ratio. This is due to the fact that the main contribution to diffraction is coming from $q\overline{q}$ pairs with larger transverse separation, r, than in the inclusive process. In the diffractive case, a similar integration as in eq. 17 leads only to a higher twist contribution. A leading twist contribution can be obtained if the dr^2 integration is extended beyond the $1/Q^2$ limit. However, at these large transverse distances saturation starts to damp the growth of the diffractive cross section [21].

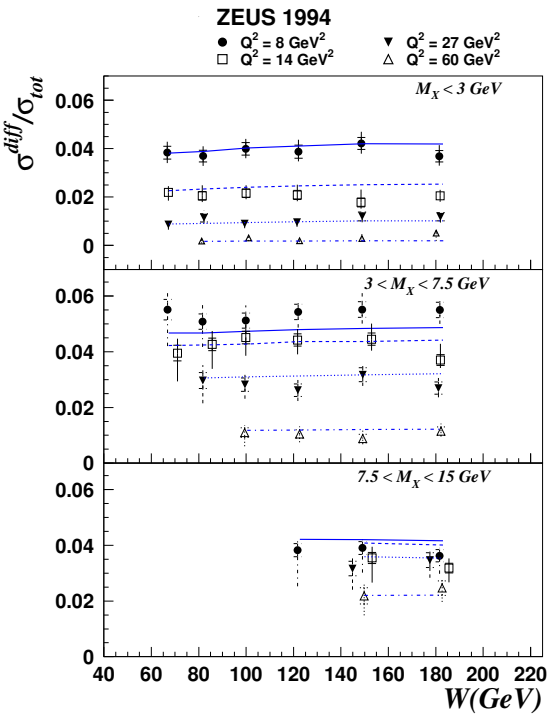

Fig. 17. The ratio of the diffractive and the total cross sections compared with the prediction of the saturation model (solid line).

4 Conclusions

The first round of experimental data on diffraction at HERA has lead to a growing theoretical understanding of relations between the, previously disconnected, phenomena of photoproduction, deep inelastic scattering and diffraction. Perturbative QCD has served as a useful guide into the transition region between hard and soft phenomena.

In the near future HERA experiments can be expected to provide a much larger body of data on diffraction. These should help to understand diffraction in deep inelastic scattering, especially in the transition region between the perturbative and nonperturbative regimes.

5 Acknowledgments

It is a pleasure to thank the organizers, G. Grindhammer, B. Kniehl and G. Kramer for a stimulating and enjoyable workshop. I have considerably benefited from discussions with J. Bartels, E. Levin, A.H. Mueller, G. Wolf and M.

Wüsthoff. I am grateful to G. Wolf for a critical reading of the manuscript and for many comments.

References

1. R.P. Feynmann, "Photon-Hadron Interactions", Benjamin, N.Y. (1972), lectures 50-54.
2. ZEUS Collab., M. Derrick et al., Z. Phys. C70 (1996) 391.
3. ZEUS Collab., J. Breitweg et al., E. Phys. J. C6 (1999) 43.
4. ARIADNE 4.0 Program Manual, L. Lönnblad, DESY-92-046 (1992), Computer Phys. Comm. 71 (1992) 15.
5. H1 Collab., C. Adloff et al., Z. Phys. C76 (1997) 613.
6. ZEUS Collab., J. Breitweg et al., E. Phys. J. C1 (1998) 81.
7. N.N. Nikolaev and B.G. Zakharov, Z. Phys. C49 (1990) 607.
8. J.R. Forshaw and D.A. Ross, *QCD and the Pomeron*, Cambridge University Press, 1997.
9. J.D. Bjorken, Proc. Int. Symp. Electron and Photon Interactions at High Energies, Cornell, 1971, p. 282.
   J.D. Bjorken, J. Kogut and D. Soper, Phys. Rev. D3 (1971) 1382.
   J.D. Bjorken and J. Kogut, Phys. Rev. D8 (1973) 1341.
10. J. Bartels, J. Ellis, H. Kowalski and M. Wüsthoff, E. Phys. J. C7 (1999) 443.
11. J.R. Forshaw, G. Kerley and G. Shaw, CERN-TH/99-58.
12. W. Buchmüller and A. Hebecker, Nucl. Phys. B476 (1996) 203.
    W. Buchmüller, M.F. McDermott, and A. Hebecker, Nucl. Phys. B487 (1997) 283; *ibid.* B500 (1997) 621.
    W. Buchmüller, T. Gehrmann, and A. Hebecker, Nucl. Phys. B537 (1999) 477.
13. A. Donnachie and P.V. Landshoff, Phys. Lett. B191 (1987) 309.
14. A. Donnachie and P.V. Landshoff, Nucl. Phys. B244 (1984) 322; Phys. Lett. B296 (1992) 227.
15. ZEUS Collab., J. Breitweg et al., Eur. Phys. J. C1 (1998) 81.
16. N.N. Nikolaev and B.G. Zakharov, Z. Phys. C53 (1992) 331; M. Genovese, N.N. Nikolaev and B.G. Zakharov, JETP 81 (1995) 625; M. Bertini, M. Genovese, N.N. Nikolaev, A.V.Pronyaev and B.G. Zakharov, Phys. Lett. B422 (1998) 238.
17. M. Wüsthoff, PhD thesis, University of Hamburg, DESY 95-166.
18. M. Ryskin, Sov. J. Nucl. Phys. 52 (1990) 529.
    N.N. Nikolaev and B.G. Zakharov, Phys. Lett. B332 (1994) 177.
    E.M. Levin and M. Wüsthoff, Phys. Rev. D50 (1994) 4306.
    S.J. Brodsky et al., Phys. Rev. D50 (1994) 3134.
    J. Bartels, H. Lotter and M. Wüsthoff, Phys. Lett. B379 (1996) 239; Erratum ibid. B382 (1996) 449.
19. A.H. Mueller, 6th International Workshop on Deep Inelastic Scattering and QCD, DIS 98, (1998) 3, World Scientific.
20. K. Golec-Biernat and M. Wüsthoff, Phys. Rev., D59:014017, (1999).
21. K. Golec-Biernat and M. Wüsthoff, DTP-99-20.